Science Advances
AAAS

advances.sciencemag.org/cgi/content/full/7/12/eabd9117/DC1

Supplementary Materials for

Bioinspired mechano-photonic artificial synapse based on graphene/MoS_2 heterostructure

Jinran Yu, Xixi Yang, Guoyun Gao, Yao Xiong, Yifei Wang, Jing Han, Youhui Chen, Huai Zhang, Qijun Sun*, Zhong Lin Wang*

*Corresponding author. Email: sunqijun@binn.cas.cn (Q.S.); zhong.wang@mse.gatech.edu (Z.L.W.)

Published 17 March 2021, *Sci. Adv.* **7**, eabd9117 (2021)
DOI: 10.1126/sciadv.abd9117

This PDF file includes:

1. Materials characterization of graphene, MoS_2, and graphene/MoS_2 heterostructure

The Raman spectra of monolayer graphene grown by chemical vapor deposition (CVD) and MoS_2 obtained by mechanical exfoliation are excited by 532 nm laser. **fig. S1A** shows the typical Raman spectra of graphene with G band at ~1593 cm^{-1} and 2D band at ~2681 cm^{-1}. The peak position of G and 2D band and the 2D/G peak intensity ratio at ~2.5 indicates the monolayer and high-quality characteristics of the graphene by CVD (*51, 52*). **fig. S1B** shows two typical Raman peaks of MoS_2 are located at ~382 and ~407 cm^{-1}, corresponding to the in-plane E_{2g} mode and out-of-plane A_{1g} mode, respectively. The interval between the two peaks is 25 cm^{-1}, indicating the multilayer character of MoS_2 (*53, 54*). The thickness of the fabricated graphene/MoS_2 (Gr/MoS_2) heterostructure and patterned graphene is ~32 nm and ~1 nm, respectively, measured by atomic force microscopy (AFM) as shown in **fig.S1C**. The graphene thickness deviation from theoretical value of monolayer graphene (0.34 nm) may be due to the intrinsic non-precise measurement by AFM and imperfect substrate status.

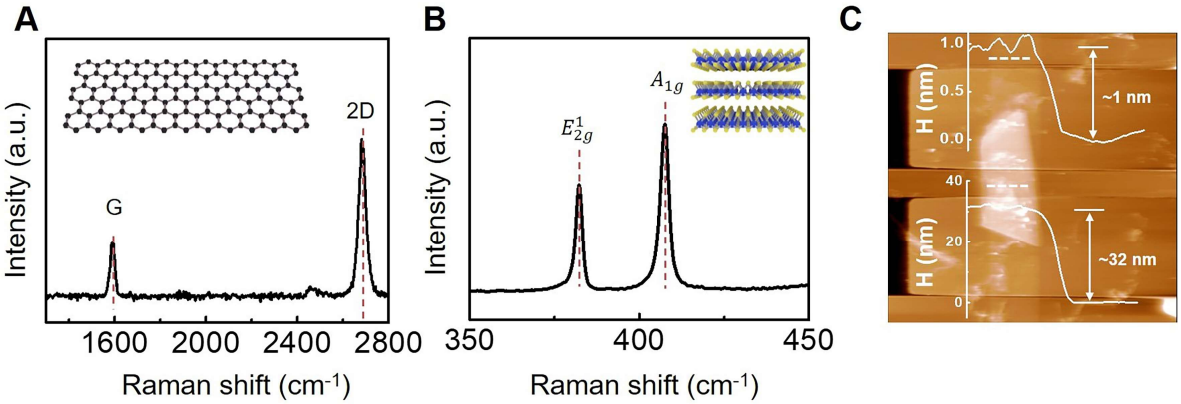

fig. S1. Materials characterization. Raman spectrum of (**A**) monolayer graphene and (**B**) multilayer MoS_2. (**C**) The AFM image of the Gr/MoS_2 heterostructure and graphene.

2. Fabrication process of the mechano-photonic artificial synapse

The mechano-photonic artificial synapse based on Gr/MoS_2 heterostructure is fabricated following the process of MoS_2 transfer, Gr/MoS_2 heterostructure construction, graphene patterning, source and drain electrodes (Cr/Au) deposition and integration of triboelectric nanogenerator (TENG) component.

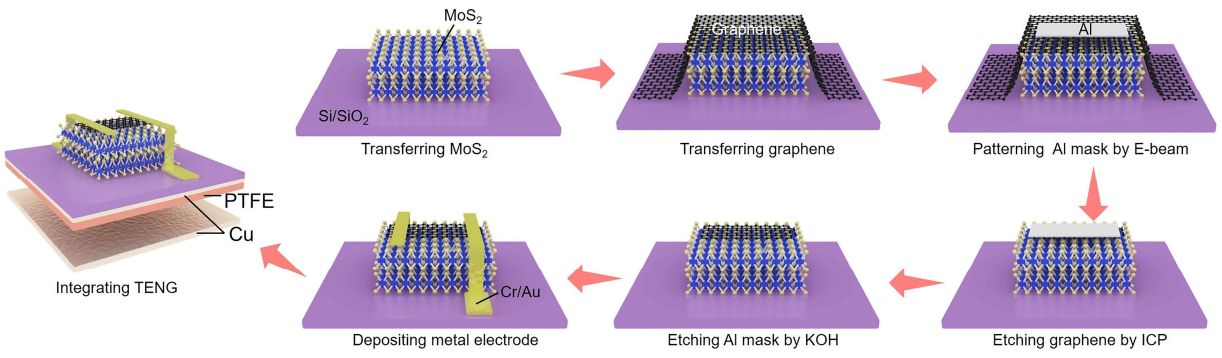

fig. S2. The fabrication process of the mechano-photonic artificial synapse based on Gr/MoS_2 heterostructure.

3. Optical image of each step for the Gr/MoS_2 transistor fabrication

Few-layer MoS_2 is firstly mechanically exfoliated and transferred onto the SiO_2/Si substrate by typical thermal transfer process. CVD graphene is transferred onto the MoS_2 flakes through polymethyl methacrylate (PMMA)-assisted wet transfer method. Then, the graphene is patterned by standard electron-beam lithography (EBL) process followed with e-beam deposition of ~15 nm Al metal layer (etching protective mask). After oxygen plasma etching, graphene is patterned into the strip shape (3×20 μm^2). Thus, the desired Gr/MoS_2 heterostructure is achieved. To fabricate the optoelectronic transistor, Cr/Au source-drain electrodes (10/40 nm) are defined on the prepared Gr/MoS_2 heterostructure by EBL and standard lift-off process assisted with PMMA sacrifice layer. Notably, although the cover area between Gr and MoS_2 in **fig. S3** and **fig. S1** is different, the channel width and channel length of transistor between source and drain electrodes are almost same, which mainly determine the device-to-device electrical performances. Besides, graphene conductance (which is higher than MoS_2 conductance in this work) dominates the device current in the heterostructure, which is patterned into the same size by photolithography in each device. Furthermore, as the source-drain electrodes are selectively and precisely patterned on the Gr/MoS_2 heterostructure, the total cover area between Gr and MoS_2 beyond the channel region does not directly affect the electrical performances among different devices.

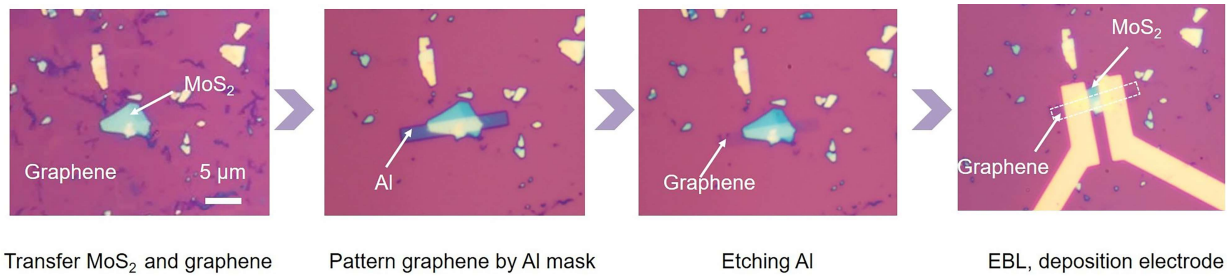

fig. S3. The optical image of each step for transistor fabrication.

4. Working mechanism of the TENG coupled to transistor

As shown in **fig. S4A**, when Cu approaches to polytetrafluoroethylene (PTFE), some surface states in the bandgap of PTFE will be filled by electrons transferred from the Cu to the PTFE, inducing negative charges on the PTFE layers and positive charges on the Cu movable layer. Then we conduct a grounding process to release the transferred charges on Cu and PTFE friction layers. The TENG component enters an electrostatic equilibrium state, delivering no output voltage ($V_{TENG} = 0$) coupling to the transistor. The relative position between PTFE and movable Cu layer is considered as the initial preset position, defined as $D_0 = 0$. When the two friction layers separate from the preset position (i.e., the movable Cu electrode moves to the right side, defined as D+, **fig. S4B**), the electrostatic equilibrium state will be broken. The negative charges on the intrinsically electronegative PTFE are lack of restriction by the counter movable Cu electrode. Then the negative charges will be coupled to the transistor gate, equivalent to applying a negative gate voltage ($-V_{TENG}$). In contrast, when the two friction layers further approach to each other from the preset position D_0 (i.e., the movable Cu layer moves to the left, defined as D-, **fig. S4C**), more negative charges are induced on the electronegative PTFE surface and attracted to side of the movable Cu friction layer. The left positive charges on PTFE are then coupled to the transistor gate through the connected Cu electrode (PTFE/Cu friction layer). In this D- state, it is equivalent to applying a positive gate voltage ($+V_{TENG}$).

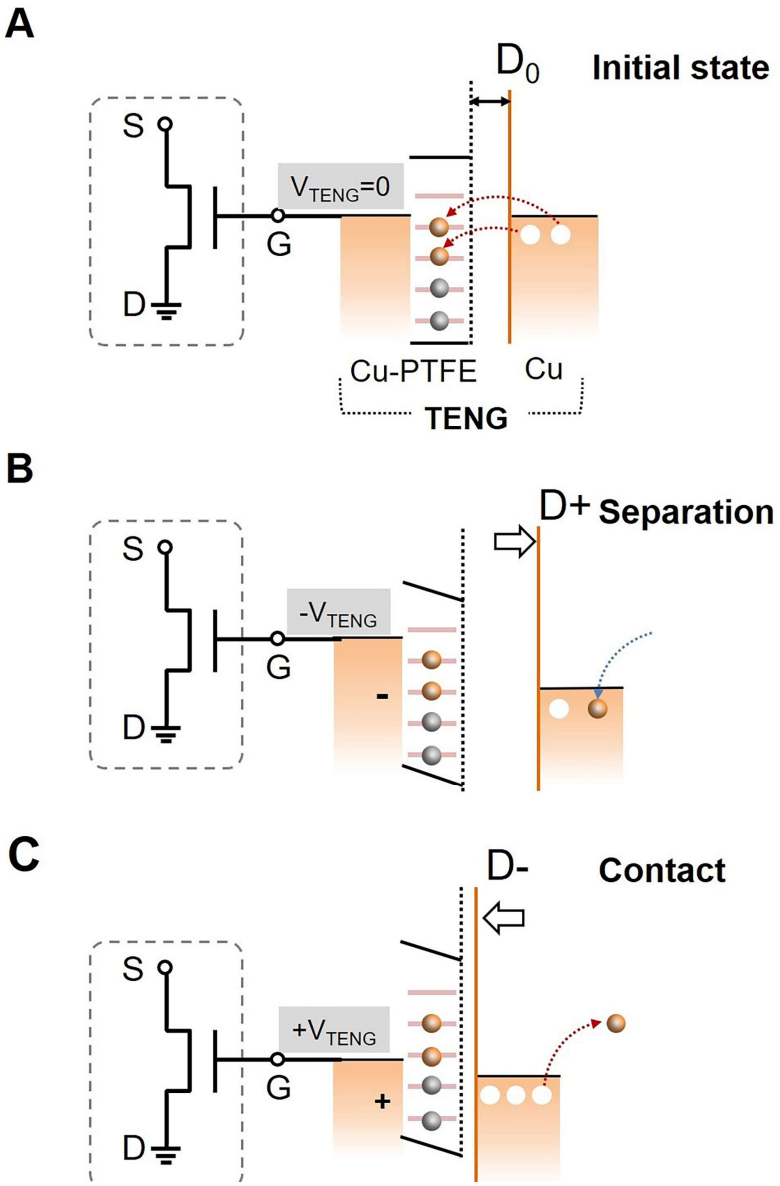

fig. S4. Working mechanism of the TENG coupled to transistor. (**A**) Initial state (D_0), no output voltage (V_{TENG} = 0) coupling to the transistor. (**B**) Separation state (D+), equivalent to applying a negative gate voltage (-V_{TENG}) to the transistor. (**C**) Contact state (D-), equivalent to applying a positive gate voltage (-V_{TENG}) to the transistor.

5. Optoelectronic characteristics of the Gr/MoS_2 transistor

The optoelectronic Gr/MoS_2 transistor exhibits excellent electrical performances. Schematic illustration of the Gr/MoS_2 heterostructure transistor is shown in **fig. S5A**. Obvious differences between the source-drain currents (I_{DS}) under light illumination (green LED, wavelength 525 nm) and dark state are shown in **fig. S5B**. Under the applied gate voltage (V_G) of -40 V, I_D under light illumination is lower than that under dark state, which can be attributed to the following reason. Under negative V_G, the transport behavior of graphene is mainly determined by the holes. Light illumination induces the photogenerated electrons in MoS_2 transfer to the holes-doped graphene so as to increase the graphene resistance and decrease the output current. The transfer curve of the Gr/MoS_2

heterostructure transistor at dark condition is shown in **fig. S5C** (black curve), which exhibits different behaviors compared to pristine graphene or MoS_2 device. When the device is illuminated with a continuous green light, the current level shows a decrement trend in the region of $V_G < V_T$ compared with I_D in dark state. Stronger light intensity leads to weaker I_D. Here, V_T is the MoS_2 conduction threshold, defined by the intersection between x-axis and the reverse extension of MoS_2 transfer curve (in dark state). In contrast, I_D has no significant change in the region of $V_G > V_T$, regardless of the light intensity. This is because the underlying MoS_2 exhibits prominent conductivity beyond V_T, which leads to an electrostatic screen effect on the photogenerated electrons transfer/exchange behavior in the Gr/MoS_2 heterostructure. The transfer curve of graphene in the dark is shown in **fig. S5D**. The Dirac voltage of graphene occurs near zero.

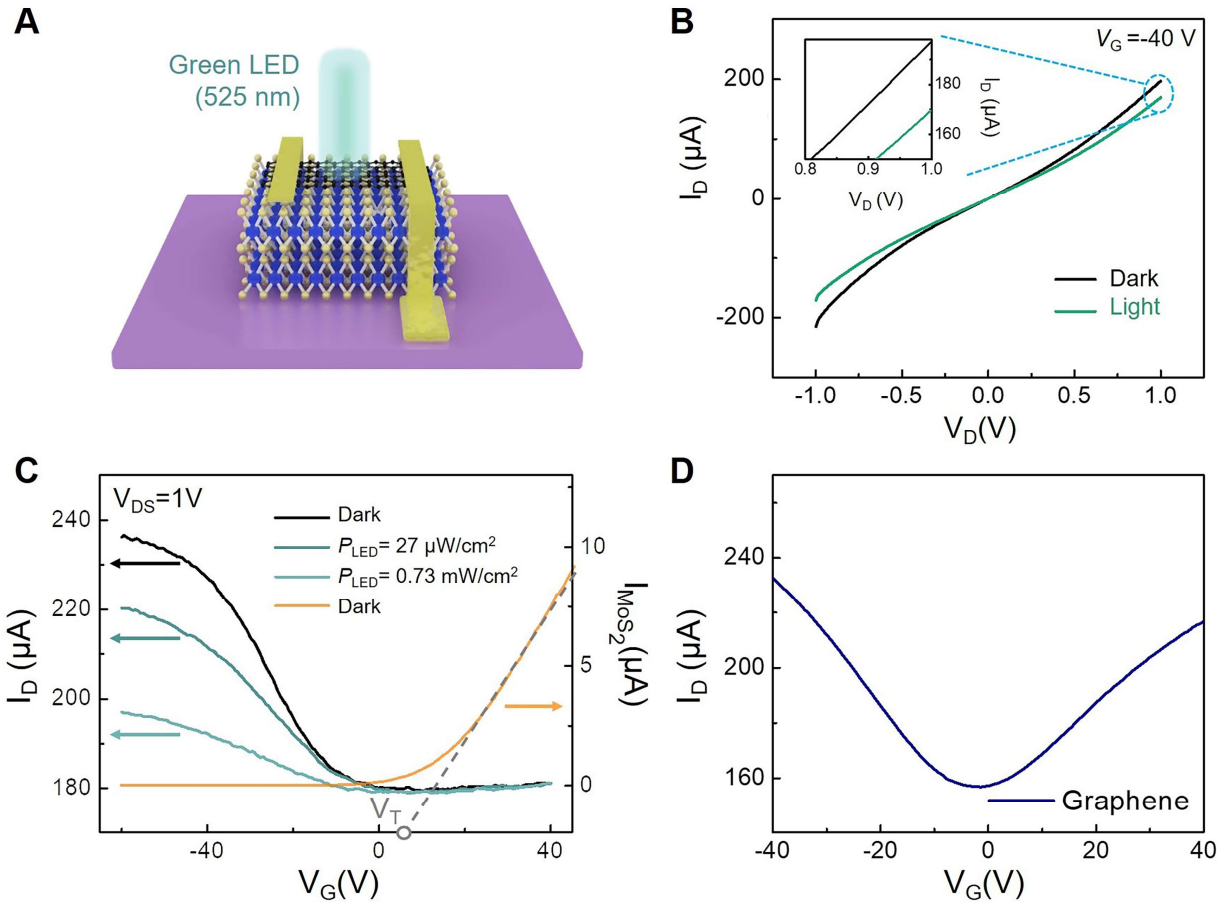

fig. S5. The basic optoelectronic characteristics of the Gr/MoS_2 heterostructure transistor. (**A**) Schematic illustration of the Gr/MoS_2 heterostructure transistor illuminated with a green light-emitting diode (LED, wavelength 525 nm). (**B**) Output characteristics of the Gr/MoS_2 transistor in dark state (black curve) and under continuous illumination by the green LED (green curve), the photoexcitation intensity (P_{LED}) is 0.73 mW·cm^{-2}. (**C**) Transfer characteristics of Gr/MoS_2 transistor in the dark and under light illumination at P_{LED} = 27 mW·cm^{-2} and P_{LED} = 0.73 mW·cm^{-2}. The yellow curve corresponding to the right y-axis is the transfer curve of pristine MoS_2 transistor under dark state. We plot the I_D of MoS_2 transistor in linear scale versus V_G to extract the MoS_2 conduction threshold (V_T). (**D**) Transfer curve of pure graphene channel in the dark.

6. Photocurrent and photoresponsivity of Gr/MoS_2 heterostructure transistor

The photocurrent (I_P) of Gr/MoS_2 transistor is defined as the current difference between the I_D in dark state and I_D under light illumination. Higher light intensity induces more photogenerated electrons transfer from MoS_2 to the holes-doped graphene (under negative V_G), which increases the resistance of graphene and leads to the current decrement (reflected as a negative I_P) under light illumination. Consequently, I_P decreases from -2.4 to -46 μA with P_{LED} increased from 0.9 μW·cm^{-2} to 13.2 mW·cm^{-2} at an applied V_G of -40 V (**fig. S7A**). The I_P level shows an enlarged variation range with the decreased V_G, which can be attributed to that more heavily holes-doped graphene under more negative V_G (e.g., V_G = -40 V) delivers more space/opportunities to be interfered by the photogenerated electrons from MoS_2. The photoresponsivity (γ) of the transistor, indicating the photoresponse under different light intensities, can be evaluated from the equation of $\gamma = I_P/P_{LED}$. Here, the γ of the Gr/MoS_2 heterostructure transistor approximates to the maximum value of 4.4×10^7 A/W at V_G = -40 V, drain voltage V_D = 1 V, and P_{LED} = ~10 mW·cm^{-2} (**fig. S7B**). The γ is determined by both V_G and P_{LED} according to the results in **fig. S7B**. Under the same P_{LED}, γ increases from 1.8×10^7 to 4.4×10^7 A/W with V_G decreased from -20 to -40 V. This is attributed to that more heavily holes-doped graphene at smaller V_G is more susceptive to the photogenerated electrons transferred from MoS_2, resulting in the relatively larger I_P. On the other hand, γ exhibits a decrement trend with increased P_{LED} at the same V_G. This phenomenon can be explained by the relatively smaller magnitude of the photocurrent (few tens) under light illumination compared to the much larger variation range of P_{LED} (10^4 orders of magnitude).

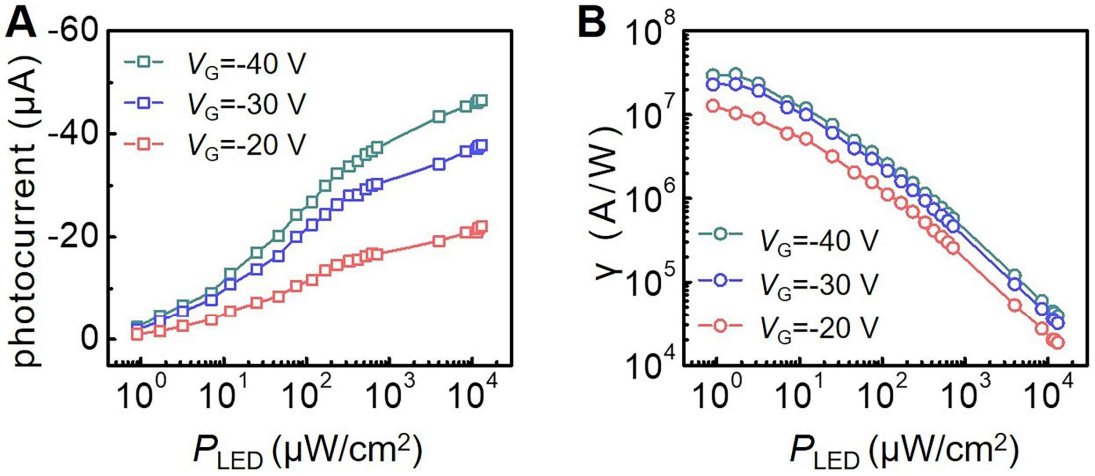

fig. S6. Photocurrent and photoresponsivity of Gr/MoS_2 heterostructure transistor. (**A**) The photocurrent and (**B**) photoresponsivity γ of the Gr/MoS_2 heterostructure transistor vs. P_{LED} at different V_Gs.

7. MoS_2 thickness influence on the photocurrent and photoresponsivity

We prepared a control sample of Gr/MoS_2 heterostructure transistor with thicker MoS_2 layer (> 50 nm), both the electric performances and photoresponses are observed to be related with heterostructure thickness (**fig. S6**). The photoresponse is obviously smaller than that in the 32 nm thick Gr/MoS_2 heterostructure. The properties of persistent photoconductivity, which are mainly determined by the physical separation of the electrons and holes by the interfacial (or potential) barrier within the heterostructures, may also be significantly

influenced due to the exponentially decreased direct tunnelling current in the heterojunction with larger thickness (*55*). When MoS_2 layer number in the heterostructure is smaller (e.g., reduced to two layer), the electric field-induced interface barrier will be suppressed, which also leads to the weakened photoresponsivity and persistent photoconductivity (*39*). Accordingly, the optimization of MoS_2 thickness in the heterostructure is critical to the device photosensitivity and electrical performances, which can potentially influence the eventual device-level or system-level applications of Gr/MoS_2 heterostructure.

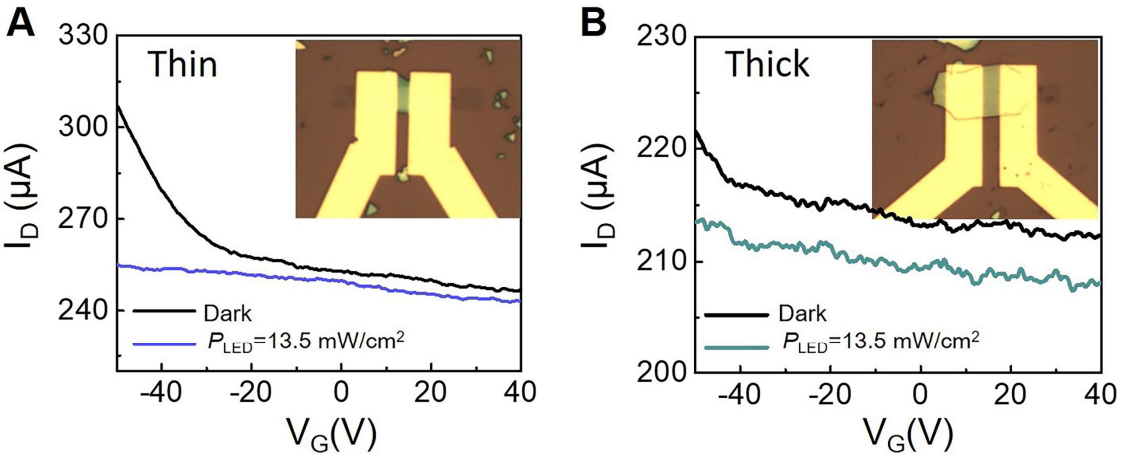

fig. S7. The optoelectronic characterization of Gr/MoS_2 transistors with different MoS_2 thicknesses. (**A**) Thin. (**B**) Thick.

8. The output characteristics of mechano-optoelectronic Gr/MoS_2 transistor

To characterize the mechano-optoelectronic transistor, the output performances are measured under the synergistic effects of TENG displacement and light illumination states as shown in **fig. S8** (dark state, P_{LED} = 27 μW·cm^{-2}, and P_{LED} = ~0.73 mW·cm^{-2} states). In the dark state (**fig. S8B**), I_D shows an obvious increment (from 328 to 386 μA) with increased TENG displacement (D, from -1.5 to 1.5 mm stepped by 0.25 mm) at V_D = 1 V. Under light illumination at P_{LED} = 27 μW·cm^{-2} (**fig. S8C**), I_D increases from 327 to 362 μA with the same variation of D. In contrast, under light illumination at P_{LED} = ~0.73 mW·cm^{-2} (**fig. S8D**), I_D shows no obvious variation under the triboelectric potential modulation with D varies from -1.5 to 1.5 mm (stepped by 0.25 mm). This may be attributed to that the more photogenerated electrons are induced in MoS_2 under stronger light illumination, which screen partial of the triboelectric potential and weaken its gating efficiency on graphene channel.

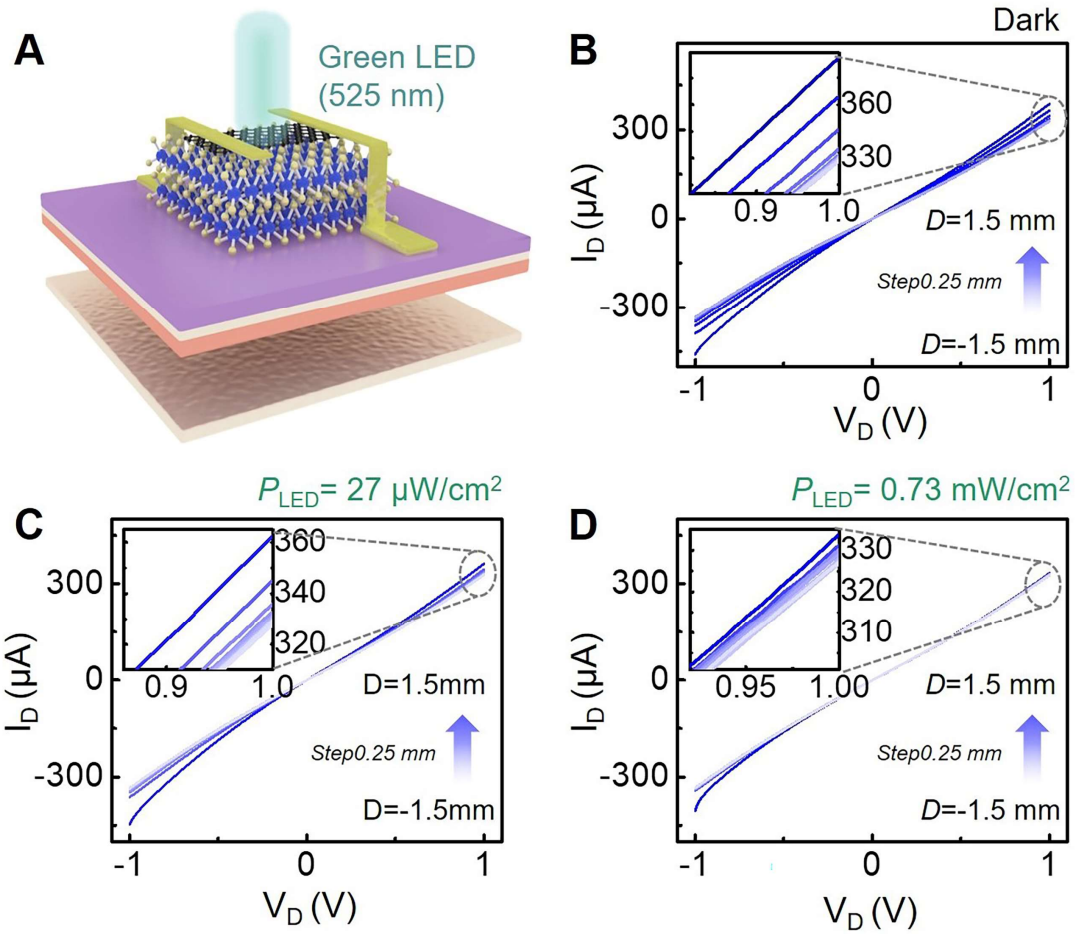

fig. S8. The output characteristics of the mechano-optoelectronic transistor based on graphene/MoS_2 heterostructure. (**A**) Schematic diagram of the mechano-optoelectronic transistor illuminated with a green LED. Output curves in dark state (**B**), under light illumination at P_{LED} = 27 μW·cm^{-2} (**C**), and at P_{LED}= 0.73 mW·cm^{-2} (**D**), with V_D from -1 to 1 V and D from -1.5 to +1.5 mm stepped by 0.25 mm.

9. Photocurrent and photoresponsivity of mechano-optoelectronic Gr/MoS_2 transistor

To further desmonstrate the synergistic effect of TENG displacement and light illumination, the influence of mechanical displacement D on the photocurrent and photosensitivity is investigated in **fig. S9**. Under the light illumination at P_{LED} = 11.5 mW·cm^{-2}, the photocurrent increases from -1.4 to -53.4 μA with D increased from 0.5 to 1.5 mm stepped by 0.25 mm. The calculated photosensitivity also shows an increment tendecy with the increased D, varying from 2.4×10^4 to 9.3×10^5 A/W. Larger displacement (D+), equivalent to applying more negative V_G, induces higher photocurrent and photoresponsivity due to the electrostatic field dependent Fermi level and electronic states in the heterostructure. These results indicate the mechano-optoelectronic Gr/MoS_2 transistor has a tunable photoresponse related with the mechanical displacement (intrinsically tuned by the induced triboelectric potential). The synergistic modualtion on the optoelectronic properties of the transistor by mechanical displacement and light illumination is the foundation of mix-modal and cross-modal plasticization in synaptic devices.

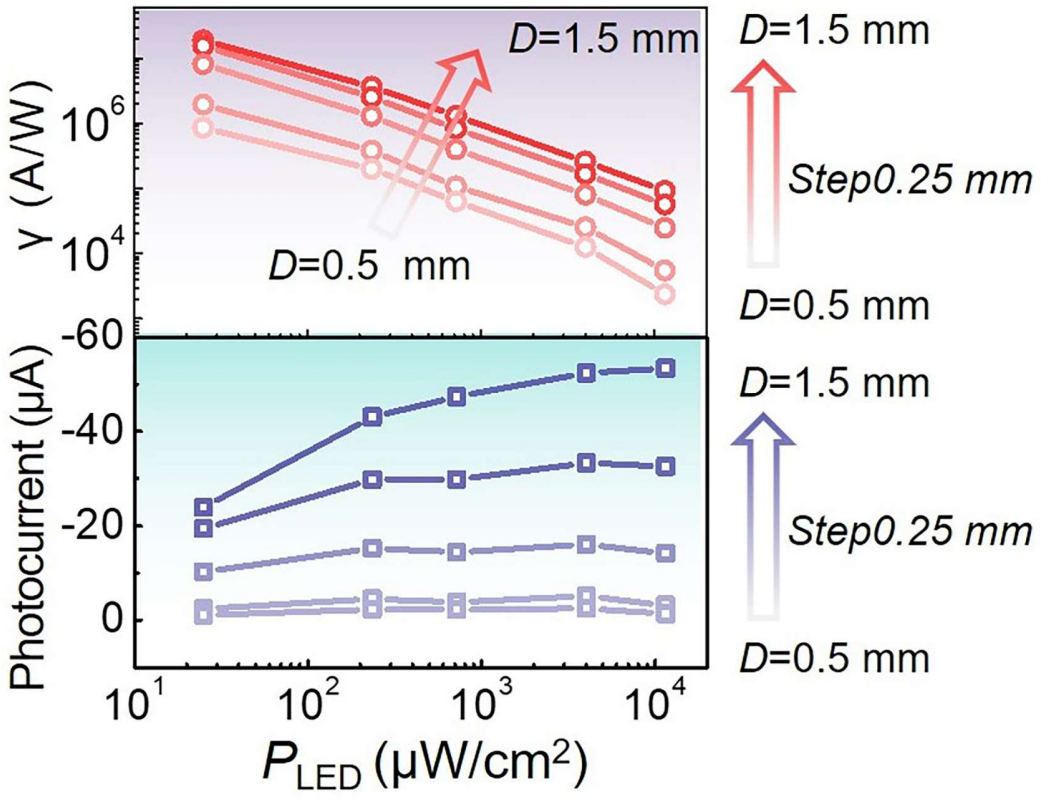

fig. S9. The photocurrent (bottom) and photoresponsivity γ (top) vs. P_{LED}, D varies from 0.5 to 1.5 mm stepped by 0.25 mm.

10. Decay time evaluation of mechano-optoelectronic Gr/MoS_2 transistor

To distinguish from the retention time, the decay time (τ) for the post synaptic current (PSC) is defined as the time of PSC decreasing from the peak current to the steady current level, which can be fitted by the typical exponential decay model with the following equation:

$$I(t) = I_{\infty} + (I_{\text{peak}} - I_{\infty}) \cdot \exp\left[\left(\frac{-(t-t_0)}{\tau}\right)^{\beta}\right],$$

where τ is the decay time, t_0 is the time at which the presynaptic spike finishes, β is the correction factor (here $\beta = 0.5$, which can be well fitted), I_{peak} is the amplitude of the EPSC, and I_{∞} is the steady value of the decay current.

To evaluate the decay time, we measured a series of post synaptic currents under different displacements and different illumination powers, respectively (**fig. S10**).

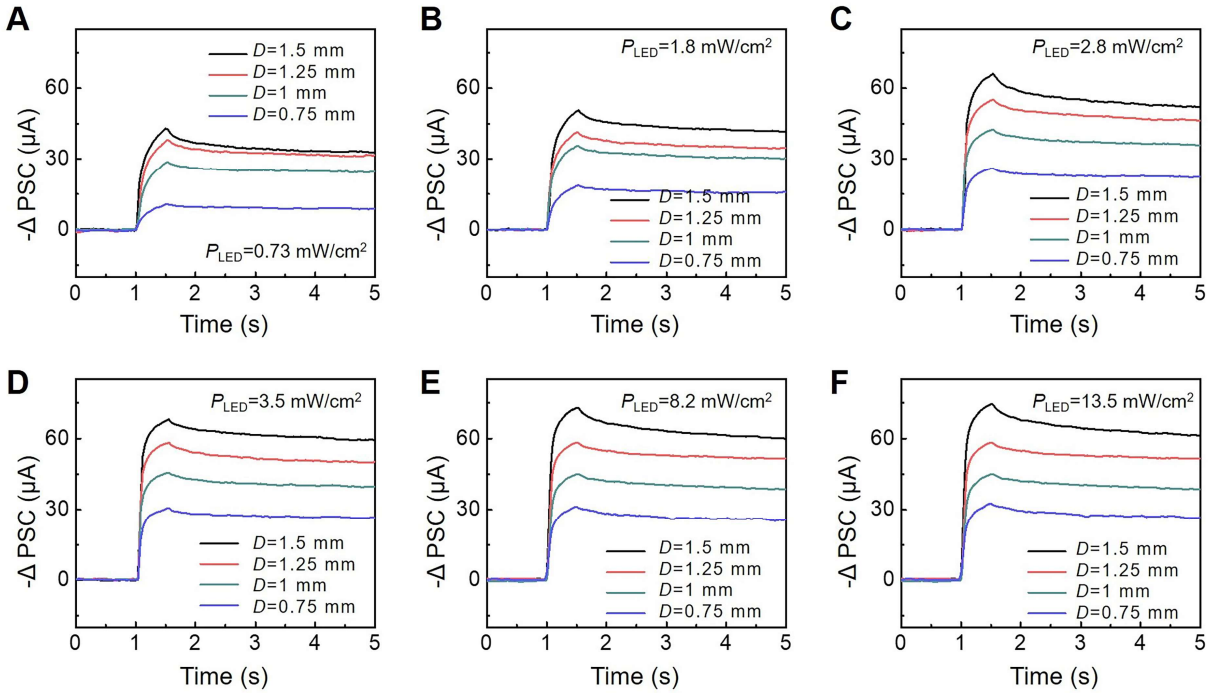

fig. S10. The -ΔPSCs under different displacements and different illumination powers. (**A**) P_{LED}=0.73 mW·cm^{-2}. (**B**) P_{LED}=1.8 mW·cm^{-2}. (**C**) P_{LED}=2.8 mW·cm^{-2}. (**D**) P_{LED}=3.5 mW·cm^{-2}. (**E**) P_{LED}=8.2 mW·cm^{-2}. (**F**) P_{LED}=13.5 mW·cm^{-2}.

11. 3D plotting of decay time versus both displacement and light illumination power

The decay time τ for the post synaptic current is plotted as a function of both displacement and illumination power, as shown in **fig. S11**. When the illumination power is 13.5 mW·cm^{-2}, the decay time increases from 3.33 to 4.47 s with displacement increased from 0.75 to 1.5 mm. When the displacement is fixed at 1 mm, the decay time increases from 0.96 to 4.31 s with the illumination power increased from 0.73 mW·cm^{-2} to 13.5 mW·cm^{-2}.

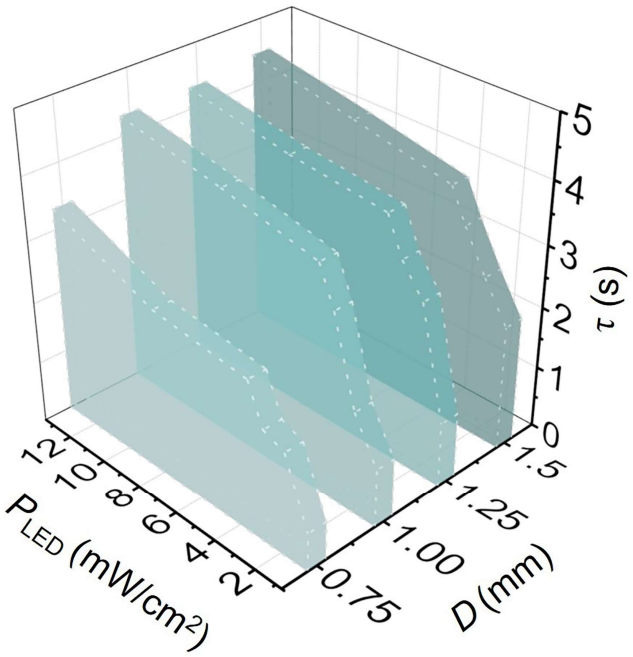

fig. S11. 3D plotting of decay time vs. displacement and light illumination power.

12. Retention time of the mechano-photonic artificial synapse

To evaluate the retention time, the postsynaptic currents at different voltages under P_{LED} = 3.5 mW·cm^{-2} are measured in **fig. S12.** The intrinsic retention time of the mechano-photonic artificial synapse is evaluated to be capable of retaining for over one hour without significant changes, which also shows potential to be retained for longer time estimated from the curves (consistent with the near-perfect charge retention in previous report (*39*)).

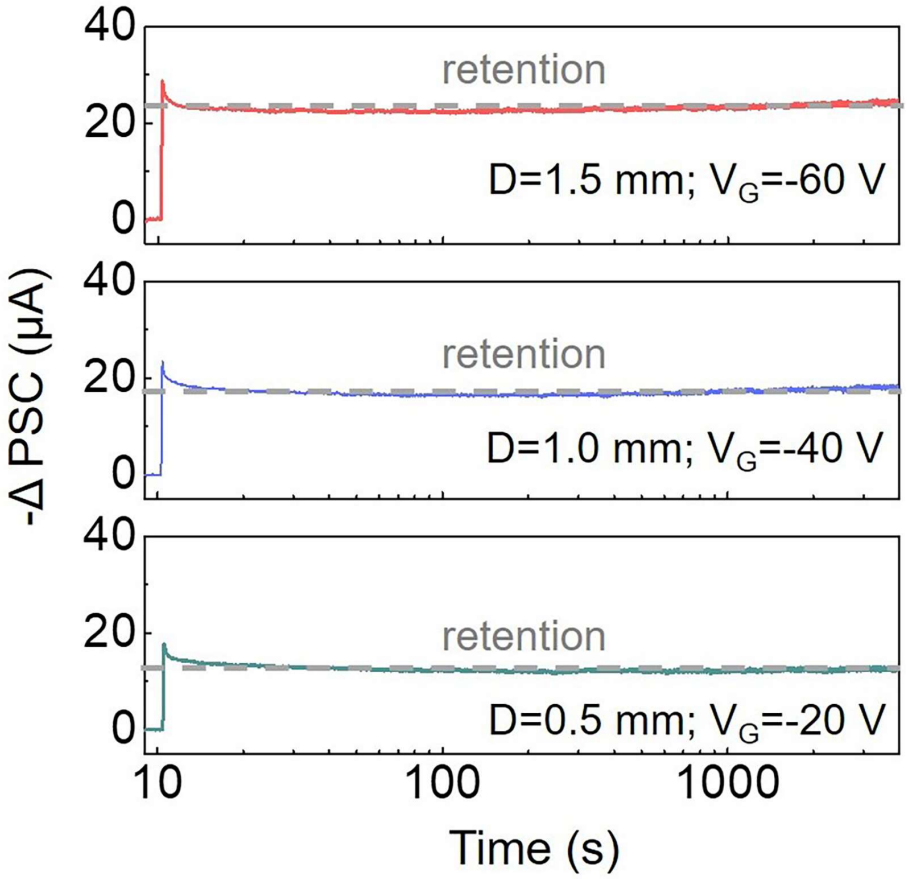

fig. S12. Retention time of the mechano-photonic artificial synapse.

13. Band diagram of mechano-optoelectronic Gr/MoS_2 transistor after switching off light

Under *D*+ state (negative triboelectric potential), the equivalent negative V_G applied to the transistor shifts the Fermi level of graphene downwards. In this state, holes dominantly contribute to the transport properties of graphene. The light illumination induces the electron-hole pairs to separate in MoS_2 and thereby pulls its energy band downward. The photogenerated electrons in MoS_2 are driven to graphene due to the equivalent negative V_G applied to the device. When the light is switched off, a small portion of the transferred electrons reversely diffuse to MoS_2 and lead to a slight recovery of I_D as shown in **Fig. 3b**. The subsequently persistent I_D arises from the potential barrier against the reverse diffusion of photogenerated electrons due to the graphene-on-MoS_2 heterostructure.

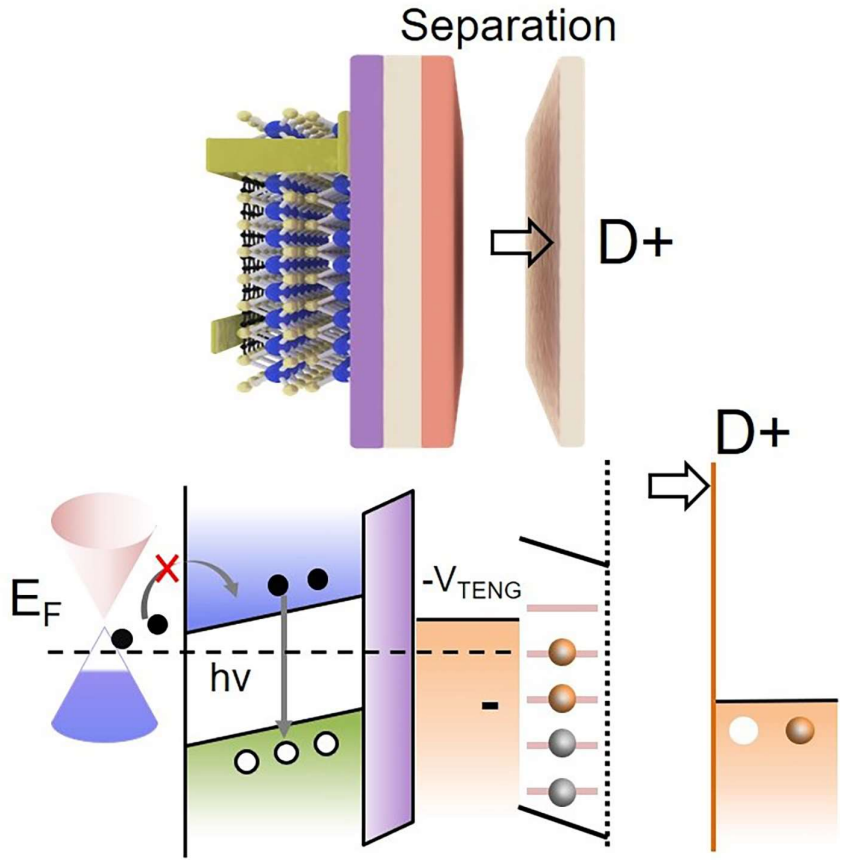

fig. S13. Schematic illustration of the band diagram when the light is turned off.

14. Postsynaptic currents (PSCs) at applied displacement smaller than 0.5 mm

When the applied $D+$ is smaller than 0.5 mm and gradually decreases, the equivalent V_G tends to increase to be positive and approach V_T (the MoS_2 conduction threshold). The MoS_2 starts to exhibit significant transport properties, which suppress the injection of photogenerated electrons to graphene. As a consequence, the postsynaptic currents (PSCs) exhibit slight variation (i.e., -ΔPSC). At applied different D (0.5, 0.25 and 0 mm), the peak value of -ΔPSC is decreased from 7 to 1 μA, with almost no obvious PSC change at $D = 0$.

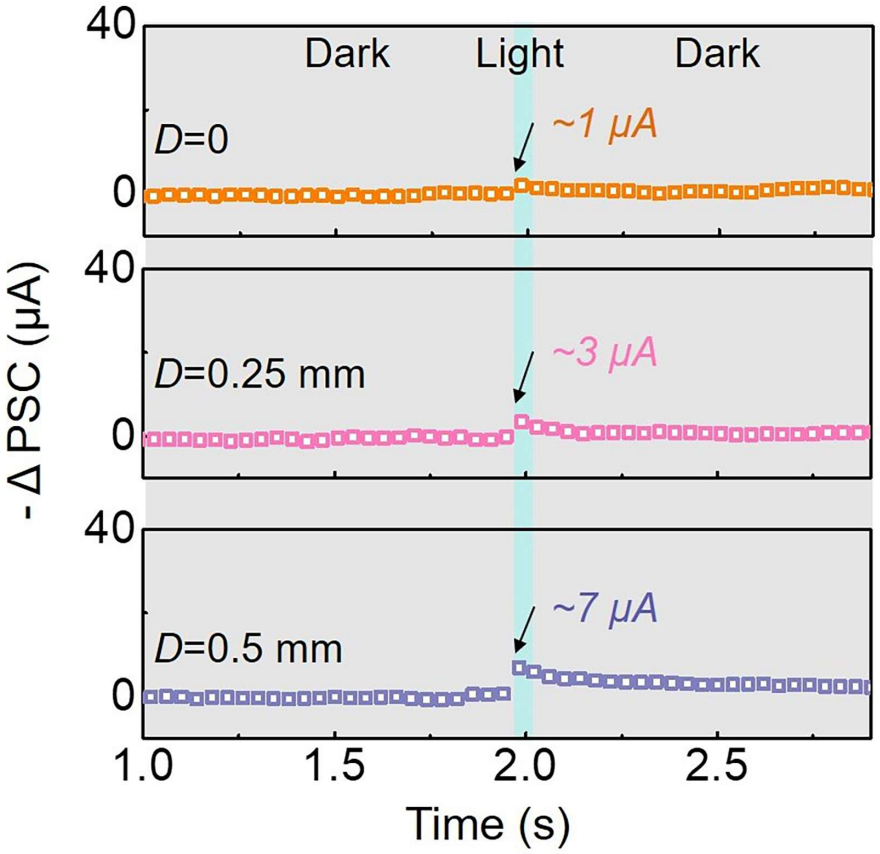

fig. S14. The PSC response of the mechano-photonic artificial synapse at fixed D of 0.5, 0.25, and 0 mm. The applied P_{LED} is 3.5 mW·cm^{-2} with pulse width at 0.5 s.

15. The erasing process of persistent PSC by TENG contact pulse (*D*-)

The persistent PSC of mechano-photonic artificial synapse can be readily erased by applying TENG contact pulse (D-), which is equivalent to applying more positive V_G. As shown in **fig. S15**, different PSCs achieved under the synergetic modulation of light pulse (P_{LED} = 3.5 mW·cm^{-2}, pulse width 0.1 s) and different D+ statuses (0.5, 1, and 1.5 mm) are successfully erased by applying D- pulse. This is because the coupled positive triboelectric potential under D- pulse instantaneously raises the Fermi energy over V_T and redistributes the charge carriers in Gr/MoS_2 heterostructure.

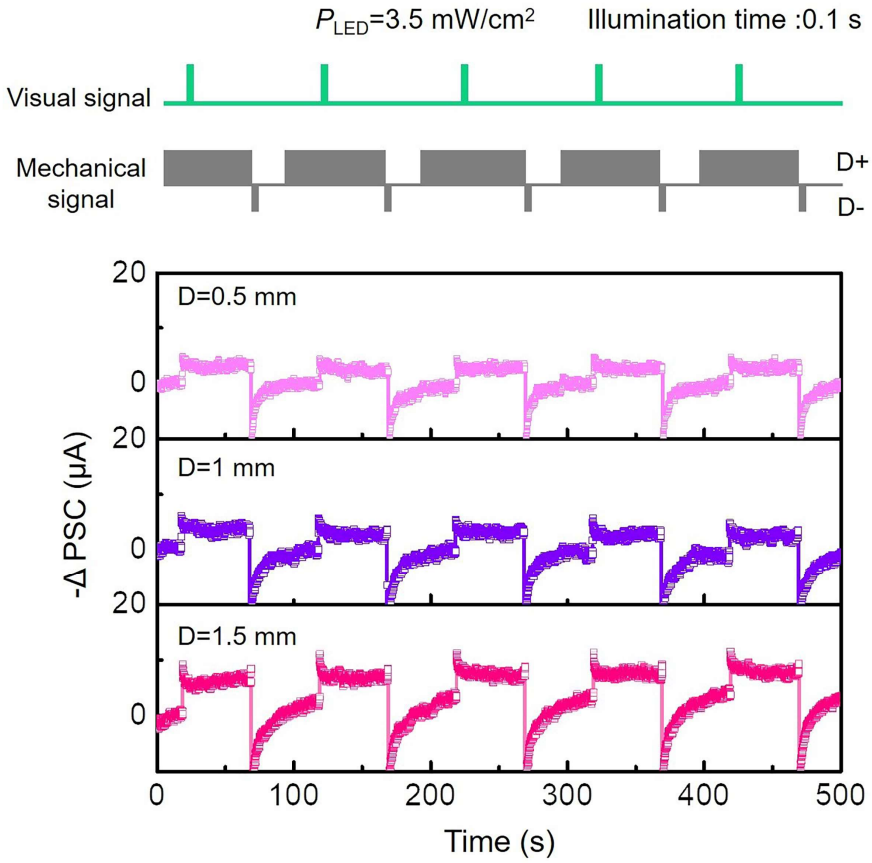

fig. S15. The erasing process of persistent PSC by TENG contact pulse (*D*-).

16. -ΔPSC of the synaptic device under forty consecutive light pulses at D = 1 mm

When forty consecutive light pulses (P_{LED} = 3.5 mW·cm^{-2}, pulse width = 50 ms) are applied to the synapse device at D = 1 mm, the amplitude value of -ΔPSC gradually increases to 20 μA and tends to be stabilized at ~ 33 μA. The gain value of -ΔPSC, which is defined as A_n/A_1 (A is the amplitude of the -ΔPSC peak value), can reach132% after the stimulation of consecutive light pulses for forty times (**fig. S16**).

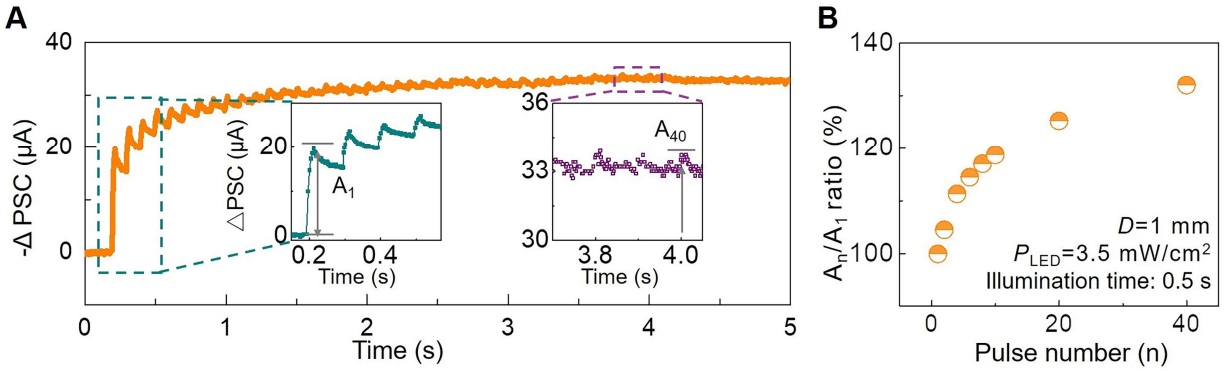

fig. S16. -ΔPSC under forty consecutive light pulses at D = 1 mm. (**A**) -ΔPSCs under forty consecutive light pulses (P_{LED} = 3.5 mW·cm^{-2}, pulse width = 50 ms, D = 1 mm). Inset: the enlarged first -ΔPSC peak A_1 (left) and last current peak A_n (right). (**B**) The current gain (defined as the ratio of A_n/A_1) vs. light pulse number.

17. Depression/potentiation (D/P) curve for artificial neural network (ANN) simulation

The D/P curve (**fig. S17**) used for ANN simulation is characterized with the variation of -ΔPSC, which is achieved by applying forty consecutive light pulses at a displacement of 1.5 mm to implement the depression process (negative increment, i.e., the depression region) and applying forty additional TENG displacement pulses (D = 0.1 mm) to implement the potentiation process (positive increment, i.e., the potentiation region). In this work, utilizing photonic depression and mechanical potentiation to achieve the D/P curve for ANN simulation is mainly attributed to the following two reasons.

Firstly, under light illumination, the drain current (I_D) of Gr/MoS_2 transistor shows a decrement tendency with the increased light intensity in the region of $V_G < V_T$. Due to the exhibited negative photoconductivity, the optical synaptic behavior of the device can only be depressed (i.e., the current is decreased under light illumination) with no potentiation behaviors under D =1.5 mm.

Secondly, based on the synergistic mechano-photonic dual-mode modulation on synaptic plasticity, we can use additional displacement pulses (D = 0.1 mm, equivalent to negative V_G) consecutively applied to the artificial synapse to modulate the carrier density in graphene channel and achieve the potentiation behaviors.

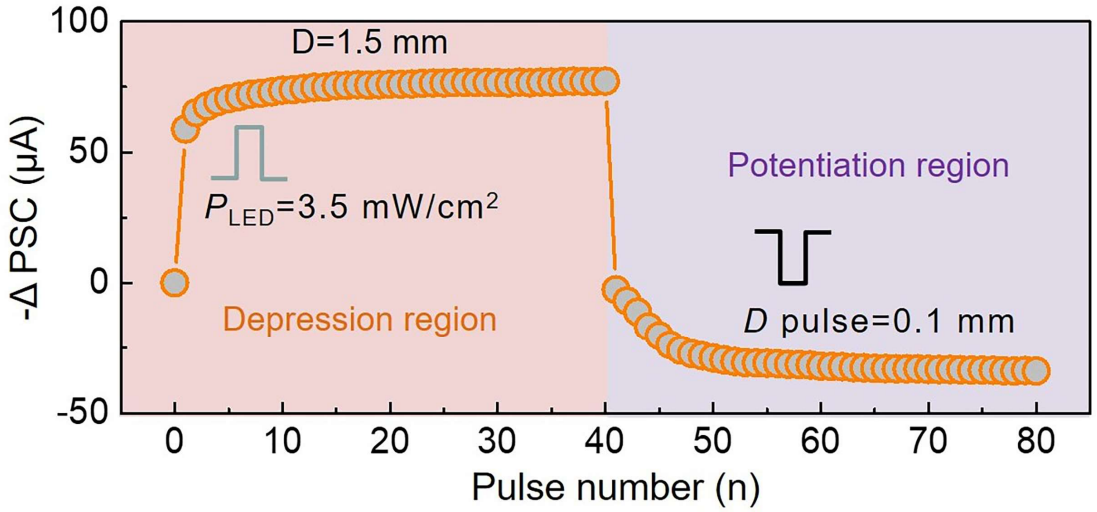

fig. S17. Depression/potentiation (D/P) curve used for ANN simulation.

REFERENCES AND NOTES

1. Y. H. Jung, B. Park, J. U. Kim, T. I. Kim, Bioinspired electronics for artificial sensory systems. *Adv. Mater.* **31**, 1803637 (2019).

2. Y. Kim, A. Chortos, W. Xu, Y. Liu, J.Y. Oh, D. Son, J. Kang, A.M. Foudeh, C. Zhu, Y. Lee, S. Niu, J. Liu, R. Pfattner, Z. Bao, T.W. Lee, A bioinspired flexible organic artificial afferent nerve. *Science* **360**, 998–1003 (2018).

3. G. C. Adam, Two artificial synapses are better than one. *Nature* **558**, 39–40 (2018).

4. V. K. Sangwan, M. C. Hersam, Neuromorphic nanoelectronic materials. *Nat. Nanotechnol.* **15**, 517–528 (2020).

5. S. Choi, S. H. Tan, Z. Li, Y. Kim, C. Choi, P. Y. Chen, H. Yeon, S. Yu, J. Kim, SiGe epitaxial memory for neuromorphic computing with reproducible high performance based on engineered dislocations. *Nat. Mater.* **17**, 335–340 (2018).

6. M. Prezioso, F. Merrikh-Bayat, B. D. Hoskins, G. C. Adam, K. K. Likharev, D. B. Strukov, Training and operation of an integrated neuromorphic network based on metal-oxide memristors. *Nature* **521**, 61–64 (2015).

7. H. Han, H. Yu, H. Wei, J. Gong, W. Xu, Recent progress in three-terminal artificial synapses: From device to system. *Small* **15**, 1900695 (2019).

8. S. Dai, Y. Zhao, Y. Wang, J. Zhang, L. Fang, S. Jin, Y. Shao, J. Huang, Recent advances in transistor–based artificial synapses. *Adv. Funct. Mater.* **29**, 1903700 (2019).

9. J. Sun, S. Oh, Y. Choi, S. Seo, M. J. Oh, M. Lee, W. B. Lee, P. J. Yoo, J. H. Cho, J.-H. Park, Optoelectronic synapse based on IGZO-alkylated graphene oxide hybrid structure. *Adv. Funct. Mater.* **28**, 1804397 (2018).

10. F. Zhou, Z. Zhou, J. Chen, T. H. Choy, J. Wang, N. Zhang, Z. Lin, S. Yu, J. Kang, H. P. Wong, Y. Chai, Optoelectronic resistive random access memory for neuromorphic vision sensors. *Nat. Nanotechnol.* **14**, 776–782 (2019).

11. M. Lee, W. Lee, S. Choi, J. W. Jo, J. Kim, S. K. Park, Y. H. Kim, Brain-inspired photonic neuromorphic devices using photodynamic amorphous oxide semiconductors and their persistent photoconductivity. *Adv. Mater.* **29**, 1700951 (2017).

12. L. Gu, S. Poddar, Y. Lin, Z. Long, D. Zhang, Q. Zhang, L. Shu, X. Qiu, M. Kam, A. Javey, Z. Fan, A biomimetic eye with a hemispherical perovskite nanowire array retina. *Nature* **581**, 278–282 (2020).

13. S. Kim, B. Choi, M. Lim, J. Yoon, J. Lee, H. D. Kim, S. J. Choi, Pattern recognition using carbon nanotube synaptic transistors with an adjustable weight update protocol. *ACS Nano* **11**, 2814–2822 (2017).

14. H. Tan, Z. Ni, W. Peng, S. Du, X. Liu, S. Zhao, W. Li, Z. Ye, M. Xu, Y. Xu, X. Pi, D. Yang, Broadband optoelectronic synaptic devices based on silicon nanocrystals for neuromorphic computing. *Nano Energy* **52**, 422–430 (2018).

15. S. Seo, S. H. Jo, S. Kim, J. Shim, S. Oh, J. H. Kim, K. Heo, J. W. Choi, C. Choi, S. Oh, D. Kuzum, H. P. Wong, J. H. Park, Artificial optic-neural synapse for colored and color-mixed pattern recognition. *Nat. Commun.* **9**, 5106 (2018).

16. M. Wang, Z. Yan, T. Wang, P. Cai, S. Gao, Y. Zeng, C. Wan, H. Wang, L. Pan, J. Yu, S. Pan, K. He, J. Lu, X. Chen, Gesture recognition using a bioinspired learning architecture that integrates visual data with somatosensory data from stretchable sensors. *Nat. Electron.* **3**, 563–570 (2020).

17. Y. Lee, J. Park, A. Choe, S. Cho, J. Kim, H. Ko, Mimicking human and biological skins for multifunctional skin electronics. *Adv. Funct. Mater.* **30**, 1904523 (2019).

18. S. Yin, C. Song, Y. Sun, L. Qiao, B. Wang, Y. Sun, K. Liu, F. Pan, X. Zhang, Electric and light dual-gate tunable MoS_2 memtransistor. *ACS Appl. Mater. Inter.* **11**, 43344–43350 (2019).

19. M. D. Tran, H. Kim, J. S. Kim, M. H. Doan, T. K. Chau, Q. A. Vu, J. H. Kim, Y. H. Lee, Two-terminal multibit optical memory via van der Waals heterostructure. *Adv. Mater.* **31**, 1807075 (2019).

20. D. Berco, D. Shenp Ang, Recent progress in synaptic devices paving the way toward an artificial cogni-retina for bionic and machine vision. *Adv. Intell. Syst.* **1**, 1900003 (2019).

21. J. Zhang, S. Dai, Y. Zhao, J. Zhang, J. Huang, Recent progress in photonic synapses for neuromorphic systems. *Adv. Intell. Syst.* **2**, 1900136 (2020).

22. H. L. Park, H. Kim, D. Lim, H. Zhou, Y. H. Kim, Y. Lee, S. Park, T. W. Lee, Retina-inspired carbon nitride-based photonic synapses for selective detection of UV light. *Adv. Mater.* **32**, 1906899 (2020).

23. L. Mennel, J. Symonowicz, S. Wachter, D. K. Polyushkin, A. J. Molina-Mendoza, T. Mueller, Ultrafast machine vision with 2D material neural network image sensors. *Nature* **579**, 62–66 (2020).

24. Z. Cheng, C. Rios, W. H. P. Pernice, C. D. Wright, H. Bhaskaran, On-chip photonic synapse. *Sci. Adv.* **3**, e1700160 (2017).

25. H. Tan, Q. Tao, I. Pande, S. Majumdar, F. Liu, Y. Zhou, P. O. A. Persson, J. Rosen, S. van Dijken, Tactile sensory coding and learning with bio-inspired optoelectronic spiking afferent nerves. *Nat. Commun.* **11**, 1369 (2020).

26. Y. Lee, J. Y. Oh, W. Xu, O. Kim, T. R. Kim, J. Kang, Y. Kim, D. Son, J. B. Tok, M. J. Park, Z. Bao, T.-W. Lee, Stretchable organic optoelectronic sensorimotor synapse. *Sci. Adv.* **4**, eaat7387 (2018).

27. D. Xiang, T. Liu, J. Xu, J. Y. Tan, Z. Hu, B. Lei, Y. Zheng, J. Wu, A. H. C. Neto, L. Liu, W. Chen, Two-dimensional multibit optoelectronic memory with broadband spectrum distinction. *Nat. Commun.* **9**, 2966 (2018).

28. F. R. Fan, L. Lin, G. Zhu, W. Wu, R. Zhang, Z. L. Wang, Transparent triboelectric nanogenerators and self-powered pressure sensors based on micropatterned plastic films. *Nano Lett.* **12**, 3109–3114 (2012).

29. Z. L. Wang, On Maxwell's displacement current for energy and sensors: The origin of nanogenerators. *Mater. Today* **20**, 74–82 (2017).

30. C. Zhang, W. Tang, L. Zhang, C. Han, Z. L. Wang, Contact electrification field-effect transistor. *ACS Nano* **8**, 8702–8709 (2014).

31. G. Gao, J. Yu, X. Yang, Y. Pang, J. Zhao, C. Pan, Q. Sun, Z. L. Wang, Triboiontronic transistor of MoS_2. *Adv. Mater.* **31**, 1806905 (2019).

32. J. Yu, X. Yang, Q. Sun, Piezo/tribotronics toward smart flexible sensors. *Adv. Intell. Syst.* **2**, 1900175 (2020).

33. G. Gao, B. Wan, X. Liu, Q. Sun, X. Yang, L. Wang, C. Pan, Z. L. Wang, Tunable tribotronic dual-gate logic devices based on 2D MoS_2 and black phosphorus. *Adv. Mater.* **30**, 1705088 (2018).

34. Y. Meng, J. Zhao, X. Yang, C. Zhao, S. Qin, J. H. Cho, C. Zhang, Q. Sun, Z. L. Wang, Mechanosensation-active matrix based on direct-contact tribotronic planar graphene transistor array. *ACS Nano* **12**, 9381–9389 (2018).

35. X. Yang, J. Yu, J. Zhao, Y. Chen, G. Gao, Y. Wang, Q. Sun, Z. L. Wang, Mechanoplastic tribotronic floating–gate neuromorphic transistor. *Adv. Funct. Mater.* **30**, 2002506 (2020).

36. Y. Liu, J. Zhong, E. Li, H. Yang, X. Wang, D. Lai, H. Chen, T. Guo, Self-powered artificial synapses actuated by triboelectric nanogenerator. *Nano Energy* **60**, 377–384 (2019).

37. H. Shim, K. Sim, F. Ershad, P. Yang, A. Thukral, Z. Rao, H.-J. Kim, Y. Liu, X. Wang, G. Gu, L. Gao, X. Wang, Y. Chai, C. Yu, Stretchable elastic synaptic transistors for neurologically integrated soft engineering systems. *Sci. Adv.* **5**, eaax4961 (2019).

38. Q. Wang, Y. Wen, K. Cai, R. Cheng, L. Yin, Y. Zhang, J. Li, Z. Wang, F. Wang, F. Wang, T. A. Shifa, C. Jiang, H. Yang, J. He, Nonvolatile infrared memory in MoS_2/PbS van der Waals heterostructures. *Sci. Adv.* **4**, eaap7916 (2018).

39. K. Roy, M. Padmanabhan, S. Goswami, T. P. Sai, G. Ramalingam, S. Raghavan, A. Ghosh, Graphene-MoS_2 hybrid structures for multifunctional photoresponsive memory devices. *Nat. Nanotechnol.* **8**, 826–830 (2013).

40. X. Chen, K. Shehzad, L. Gao, M. Long, H. Guo, S. Qin, X. Wang, F. Wang, Y. Shi, W. Hu, Y. Xu, X. Wang, Graphene hybrid structures for integrated and flexible optoelectronics. *Adv. Mater.* **32**, 1902039 (2019).

41. D. De Fazio, I. Goykhman, D. Yoon, M. Bruna, A. Eiden, S. Milana, U. Sassi, M. Barbone, D. Dumcenco, K. Marinov, A. Kis, A. C. Ferrari, High responsivity, large-area graphene/MoS_2 flexible photodetectors. *ACS Nano* **10**, 8252–8262 (2016).

42. H. Xu, J. Wu, Q. Feng, N. Mao, C. Wang, J. Zhang, High responsivity and gate tunable graphene-MoS_2 hybrid phototransistor. *Small* **10**, 2300–2306 (2014).

43. Y. Wen, P. He, Y. Yao, Y. Zhang, R. Cheng, L. Yin, N. Li, J. Li, J. Wang, Z. Wang, C. Liu, X. Fang, C. Jiang, Z. Wei, J. He, Bridging the van der Waals interface for advanced optoelectronic devices. *Adv. Mater.* **32**, 1906874 (2019).

44. L. F. Abbott, W. G. Regehr, Synaptic computation. *Nature* **431**, 796–803 (2004).

45. T. Ohno, T. Hasegawa, T. Tsuruoka, K. Terabe, J. K. Gimzewski, M. Aono, Short-term plasticity and long-term potentiation mimicked in single inorganic synapses. *Nat. Mater.* **10**, 591–595 (2011).

46. L. Q. Zhu, C. J. Wan, L. Q. Guo, Y. Shi, Q. Wan, Artificial synapse network on inorganic proton conductor for neuromorphic systems. *Nat. Commun.* **5**, 3158 (2014).

47. J. Zhu, Y. Yang, R. Jia, Z. Liang, W. Zhu, Z. U. Rehman, L. Bao, X. Zhang, Y. Cai, L. Song, R. Huang, Ion gated synaptic transistors based on 2D van der Waals crystals with tunable diffusive dynamics. *Adv. Mater.* **30**, 1800195 (2018).

48. W. Xu, S. Y. Min, H. Hwang, T. W. Lee, Organic core-sheath nanowire artificial synapses with femtojoule energy consumption. *Sci. Adv.* **2**, e1501326 (2016).

49. Y. Chen, G. Gao, J. Zhao, H. Zhang, J. Yu, X. Yang, Q. Zhang, W. Zhang, S. Xu, J. Sun, Y. Meng, Q. Sun, Piezotronic graphene artificial sensory synapse. *Adv. Funct. Mater.* **29**, 1900959 (2019).

50. H. Wang, Q. Zhao, Z. Ni, Q. Li, H. Liu, Y. Yang, L. Wang, Y. Ran, Y. Guo, W. Hu, Y. Liu, A ferroelectric/electrochemical modulated organic synapse for ultraflexible, artificial visual-perception system. *Adv. Mater.* **30**, 1803961 (2018).

51. Y. Y. Wang, Z. H. Ni, T. Yu, Z. X. Shen, H. M. Wang, Y. H. Wu, W. Chen, A. T. Shen Wee, Raman studies of monolayer graphene: The substrate effect. *J. Phys. Chem. C* **112**, 10637–10640 (2008).

52. H. Zhang, J. Yu, X. Yang, G. Gao, S. Qin, J. Sun, M. Ding, C. Jia, Q. Sun, Z. L. Wang, Ion gel capacitively coupled tribotronic gating for multiparameter distance sensing. *ACS Nano* **14**, 3461–3468 (2020).

53. H. Li, Q. Zhang, C. C. R. Yap, B. K. Tay, T. H. T. Edwin, A. Olivier, D. Baillargeat, From bulk to monolayer MoS_2: Evolution of Raman scattering. *Adv. Funct. Mater.* **22**, 1385–1390 (2012).

54. C. Lee, H. Yan, L. E. Brus, T. F. Heinz, J. Hone, S. Ryu, Anomalous lattice vibrations of single- and few-layer MoS2. *ACS Nano* **4**, 2695–2700 (2010).

55. C.-H. Lee, G.-H. Lee, A. M. Zande, W. Chen, Y. Li, M. Han, X. Cui, G. Arefe, C. Nuckolls, T. F. Heinz, J. Guo, J. Hone, P. Kim, Atomically thin p–n junctions with van der Waals Heterointerfaces. *Nat. Nanotechnol.* **9**, 676–681 (2014).